Journal of Materials Research and Technology 28 (2024) 4615–4625

Contents lists available at ScienceDirect

Journal of Materials Research and Technology

journal homepage: www.elsevier.com/locate/jmrt

Nanoindentation induced anisotropy of deformation and damage behaviors of MgF_2 crystals

Yinchuan Piao [a], Chen Li [a,b,*], Yuxiu Hu [a], Hailong Cui [c], Xichun Luo [d], Yanquan Geng [a,b,**], Feihu Zhang [a]

[a] School of Mechatronics Engineering, Harbin Institute of Technology, Harbin, 150001, China
[b] Key Laboratory of Microsystems and Microstructures Manufacturing (HIT), Harbin Institute of Technology, Harbin, 150001, China
[c] Sichuan Precision and Ultra-Precision Machining Engineering Technology Center, Chengdu, 610200, China
[d] Centre for Precision Manufacturing, DMEM, University of Strathclyde, Glasgow, G1 1XQ, UK

ARTICLE INFO

Keywords:
Anisotropy
Slip motions
Cleavage fractures
Nanoindentation
MgF_2 crystal

ABSTRACT

The competition mechanism between the slip motions and cleavage fractures is related to the anisotropy of deformation behaviors, which is essential to manufacture complex optical components. To identify competition mechanism between the slip motions and cleavage fractures and reveal the anisotropy of deformation and damage behaviors of MgF_2 crystals, the nanoindentation tests were systematically conducted on different crystal planes. In addition, the stress induced by the nanoindentation was developed and decomposed along the slip systems and cleavage planes, and cleavage factors and Schmid factors were calculated. The stress, cleavage factors and Schmid factors indicated that the activation degree of the slip motions and cleavage fractures determined the indentation morphologies. Under the same indentation conditions, the nanoindentation of the (001) crystal plane activated most slip motions, so the plastic deformation is most prone to occur on this crystal plane. The nanoindentation of the (010) crystal plane activated less slip motions and most cleavage fractures, resulting in the severest brittle fractures on the (010) crystal plane. The theoretical results consisted well with the experimental results, which provides the theoretical guidance to the low-damage manufacturing of MgF_2 components.

1. Introduction

Magnesium fluoride (MgF_2) crystal is the excellent material for the fabrication of complex optical components due to its extraordinary mechanical strength, corrosion resistance and optical properties. However, MgF_2 single crystal is the typical hard-to-machine material for high hardness, brittleness and anisotropy. Yu et al. carried out the cutting experiments of MgF_2 single crystals and distinct cracks were found on the machined surface [1]. Huang et al. conducted the scratch tests of MgF_2 single crystals, and observed significant brittle fractures on the scratch grooves [2]. Babu et al. introduced molecular dynamics simulations of the MgF_2 single crystals, and the results indicated the mechanical characteristics of MgF_2 single crystal showed distinct anisotropy [3]. In addition, the manufacturing of complex components is hindered by traditional manufacturing methods [4–7]. For inhibiting the brittle fractures and improving the manufacturing efficiency, numerous researchers have devoted to investigating the mechanical properties and manufacturing techniques of MgF_2 single crystals. The critical cutting depth model of MgF_2 single crystals was developed by Hayama based on the crack propagation of brittle materials [8]. Min et al. conducted cutting experiments of MgF_2 single crystals, and observed that the critical depth-of-cut varied with the crystal orientations [9]. Liu et al. explored the application of ultrasonic-assisted cutting tests of MgF_2 single crystals, which demonstrated that crack-free machining of the components effectively improved the manufacturing efficiency [10]. Numerous researches have proposed innovative manufacturing methods for complex MgF_2 components. However, the anisotropy of deformation behaviors of MgF_2 single crystals significantly limits the improving of the component quality and manufacturing efficiency. Revealing anisotropy of deformation behaviors of MgF_2 single crystals can provide theoretical foundation to improve the component quality and manufacturing efficiency. However, few researchers have

* Corresponding author. School of Mechatronics Engineering, Harbin Institute of Technology, Harbin, 150001, China.
** Corresponding author. School of Mechatronics Engineering, Harbin Institute of Technology, Harbin, 150001, China.
E-mail addresses: hit_chenli@163.com (C. Li), gengyanquan@hit.edu.cn (Y. Geng).

https://doi.org/10.1016/j.jmrt.2024.01.034
Received 8 December 2023; Received in revised form 30 December 2023; Accepted 5 January 2024
Available online 10 January 2024

systematically analyzed the anisotropy of deformation and damage behaviors of MgF_2 single crystals.

The nanoindentation instrument can accurately control the load in nano- and micro-scales and obtain mechanical properties and displacement-load curves. Many scholars performed the nanoindentation tests to analyze the mechanical properties and deformation behaviors. According to the nanoindentation tests, hardness, elastic modulus, fracture toughness, and maximum elastic recovery rate of YAG crystals were calculated by Li [11] et al. Liu et al. conducted the nanoindentation tests of KDP crystals under different temperatures and indicated that increasing temperature promoted the plastic deformation and suppressed brittle fractures [12,13]. Yan et al. carried out nanoindentation experiments of Si single crystals to investigate the material damage, and they observed distinct amorphous and nano-crystalline damages in the subsurface region [14]. Zhang et al. investigated the creep behavior of KDP crystals by nanoindentation tests and determined that the creep of KDP crystals was induced by the dislocation motion [15]. Csanádi et al. researched the effect of crystal orientation on the nanoindentation hardness and indentation modulus of Si_3N_4 ceramics, and developed a theoretical model based on the slip system to illustrate the anisotropy of the hardness of Si_3N_4 ceramics [16]. Due to the structural characteristics, single crystals exhibit distinct anisotropy of machined surface morphologies [17–20]. Consequently, researchers have investigated the slip systems and cleavage planes of single crystals to reveal the anisotropy of deformation behaviors. Huang et al. successfully predicted that ($[\bar{2}11]$) and $[11\bar{2}]$ crystal orientations are more prone to generate brittle fractures based on slip systems [21]. Bending tests of the sapphire were conducted by Huang et al. and the anisotropy mechanism of the fracture toughness was revealed based on the critical shear stress of different slip systems [22]. Li [23] et al. performed nanoindentation tests of single crystals to analyze the microhardness anisotropy, and observed the correlation between microhardness anisotropy and the slip systems. Kwon [24] et al. explained the anisotropy of the crack initiation and ductile machining of sapphire crystals by modifying the cleavage factor and Schmid factor. Mizumoto [25] et al. analyzed the anisotropy of the critical cutting depth during the machining of CaF_2 single crystals based on cleavage factors, and the consistent relationship between the variation of critical cutting depth and cleavage factor was derived. Many researches have indicated that the deformation behaviors were related to the stress field. Li et al. successfully predicted the direction of crack initiation and propagation locations during the characterization of brittle materials according to the stress field model [26]. Yang et al. conducted multi-abrasives machining tests and found that the crack propagation was induced by the maximum principal stress [27]. Li et al. analyzed the stress-induced plastic damages of GaN crystals through molecular dynamics simulations, and found that the laser reduced the stress and suppressed the plastic damage of GaN crystals [28,29]. Wang et al. developed the stress field model to analyze the crack propagation in the manufacturing of Si single crystals, and they observed that the radial crack was induced by the residual stress [30]. Many studies focused on analyzing the deformation behaviors based on the main stress. However, few researchers introduced the competition between the slip motions and cleavage fractures to the stress field model, and illustrated the anisotropy of deformation behaviors.

This study aims at revealing the anisotropy of deformation behaviors of MgF_2 single crystals by the competition between the slip motions and cleavage fractures. To observe the deformation behaviors on (001), (010) and (110) crystal planes, nanoindentation tests on different crystal planes of MgF_2 single crystals were carried out. The stress field models induced by the nanoindentation were developed and decomposed along the slip systems and cleavage planes, which will illustrate the anisotropy of deformation behaviors by comparing stress distributions along the cleavage planes and the slip systems. The cleavage factors and Schmid factors under different surfaces of Berkovich indenter were calculated,

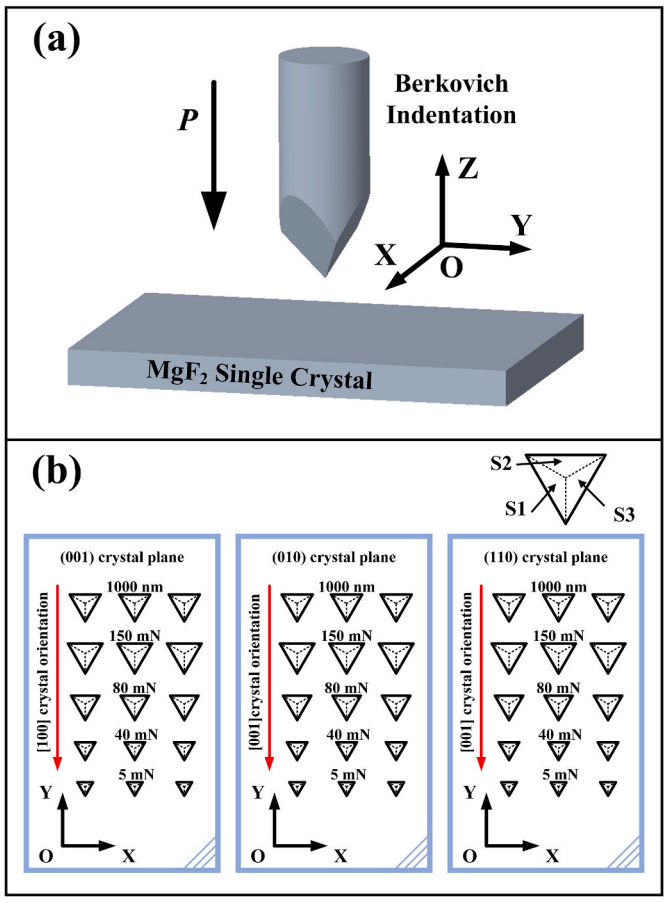

Fig. 1. Schematic diagram of (a) nanoindentation process and (b) nanoindentation tests on different crystal planes.

which will reveal the deformation mechanisms of the indentation surfaces that contact with the indenter. This paper will reveal the nanoindentation induced anisotropy of deformation and damage behaviors, and provide theoretical guidance for the manufacturing of complex MgF_2 components with high surface integrity.

2. Experimental methods and simulation models

2.1. Materials and methods

The nanoindentation tests are commonly carried out to analyze the deformation behaviors. In order to investigate the anisotropy of deformation behaviors of MgF_2 single crystals, the nanoindentation tests were performed on (001), (010) and (110) crystal planes. As shown in Fig. 1, Berkovich diamond indenter with a tip radius of approximately 100 nm was used on a nano indenter (Agilent G200, USA). The dimensions of the specimens were 10 mm × 5 mm × 2 mm. The long edges of the (001), (010) and (110) crystal planes were parallel to the [100], [001] and [001] crystal orientations, respectively. To suppress the damage generation during the preparation process of the MgF_2 specimen, chemically-mechanically polishing was used to ensure that the specimen has a surface roughness of 0.15 nm in Ra before the nanoindentation tests. A commercial colloidal silica slurry of size 25 nm was used in the polishing test. The polishing speed, specimen speed, polishing force and suspension flow rate, and polishing time are 150 rpm, 50 rpm, 10 N, 100 mL/h, and 30 min, respectively. The three contact surfaces between the specimen and Berkovich diamond indenter were marked as S1, S2 and S3, respectively. The nanoindentation tests of the continuous stiffness mode were conducted to obtain the hardness of different crystal planes, and the nanoindentation tests of the quasi-static mode were conducted

Table 1
Experimental conditions.

No.	Mode	Crystal plane	Indentation displacement and load
1–3	continuous stiffness	(001), (010), (110)	1000 nm
4–7	quasi-static	(001)	5 mN, 40 mN, 80 mN, 150 mN
8–11	quasi-static	(010)	5 mN, 40 mN, 80 mN, 150 mN
12–15	quasi-static	(110)	5 mN, 40 mN, 80 mN, 150 mN

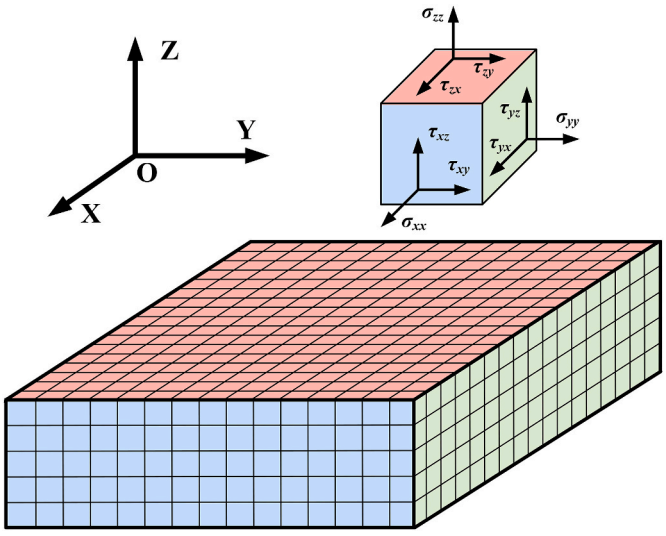

Fig. 2. Diagrammatic sketch of the stress field induced by nanoindentation.

to investigate the deformation behaviors on different crystal planes. The detailed experimental conditions of nanoindentation tests were listed in Table 1. To ensure the accuracy of the experimental results, each test was repeated three times. Indentation morphologies were observed by a scanning electron microscope (SEM, SUPRA 55 SAPPHIRE, Germany).

2.2. The development and decomposition of the stress

Wang [31] and Li [32] et al. agreed that the deformation behaviors were related to the stress field. Consequently, the stress model of the nanoindentation was developed to investigated the anisotropy of deformation behaviors. The stress filed is shown in Fig. 2.

During the nanoindentation process, the stress was induced by the normal load P. The stress field induced by the nanoindentation can be regarded as the stress field induced by a point force on a semi-infinite region. Boussinesq stress field can calculate the stress field induced by the normal point force on a semi-infinite region. Therefore, Boussinesq stress field was used to calculate the stress field induced by the normal load P, which can be expressed by Equation (1),

$$\begin{cases} \sigma_{xx} = \dfrac{P}{2\pi}\left\{\dfrac{1-2\nu_{(hkl)}}{r^2}\left[\left(1-\dfrac{z}{\rho}\right)\dfrac{x^2-y^2}{r^2}+\dfrac{zy^2}{\rho^3}\right]-\dfrac{3zx^2}{\rho^5}\right\} \\ \sigma_{yy} = \dfrac{P}{2\pi}\left\{\dfrac{1-2\nu_{(hkl)}}{r^2}\left[\left(1-\dfrac{z}{\rho}\right)\dfrac{y^2-x^2}{r^2}+\dfrac{zx^2}{\rho^3}\right]-\dfrac{3zy^2}{\rho^5}\right\} \\ \sigma_{zz} = -\dfrac{P}{2\pi}\dfrac{3z^3}{\rho^5} \\ \tau_{xy} = \dfrac{P}{2\pi}\left\{\dfrac{1-2\nu_{(hkl)}}{r^2}\left[\left(1-\dfrac{z}{\rho}\right)\dfrac{xy}{r^2}-\dfrac{xyz}{\rho^3}\right]-\dfrac{3xyz}{\rho^5}\right\} \\ \tau_{yz} = \dfrac{P}{2\pi}\dfrac{3yz^2}{\rho^5} \\ \tau_{xz} = \dfrac{P}{2\pi}\dfrac{3xz^2}{\rho^5} \end{cases} \tag{1}$$

where $\rho^2 = x^2+y^2$, $r^2 = x^2+y^2+z^2$, and $\nu_{(hkl)}$ is the poison's ratio of the (hkl) crystal plane. The poison's ratio of the (001), (010) and (110) crystal planes can be found in our previous work [33]. Mizumoto and Wang et al. indicated that slip motions and cleavage fractures were related to the deformation behaviors of single crystals [34,35]. Slip motions are induced by the shear stress along the slip systems, and cleavage fractures are induced by the normal stress along the cleavage planes. Consequently, the stress will be decomposed along the slip systems and cleavage planes.

As shown in Fig. 3, S_n is the unit normal vector of the slip plane, S_t is the unit vector of the slip direction, C_n is the unit normal vector of the cleavage plane, σ_{ts} is the total stress of slip systems, and σ_{tc} is the total stress of the cleavage plane. σ_{ts} and σ_{tc} can be expressed by Equations (2) and (3),

$$\sigma_{ts} = \begin{bmatrix} \sigma_{xx} & \tau_{xy} & \tau_{xz} \\ \tau_{yx} & \sigma_{yy} & \tau_{yz} \\ \tau_{zx} & \tau_{zy} & \sigma_{zz} \end{bmatrix} \begin{bmatrix} n_{xs} \\ n_{ys} \\ n_{zs} \end{bmatrix} \tag{2}$$

$$\sigma_{tc} = \begin{bmatrix} \sigma_{xx} & \tau_{xy} & \tau_{xz} \\ \tau_{yx} & \sigma_{yy} & \tau_{yz} \\ \tau_{zx} & \tau_{zy} & \sigma_{zz} \end{bmatrix} \begin{bmatrix} n_{xc} \\ n_{yc} \\ n_{zc} \end{bmatrix} \tag{3}$$

where n_{xs}, n_{ys} and n_{zs} are the directional cosines between the normal direction of the slip plane and X, Y and Z axis, respectively. n_{xc}, n_{yc} and n_{zc} are the directional cosines between the normal direction of the cleavage plane and X, Y and Z axis, respectively. The slip motions are induced by the stress σ_s which is along the slip systems. The cleavage fractures are induced by the stress σ_c which is perpendicular to the cleavage planes. The stresses σ_s and σ_c can be expressed by Equation (4),

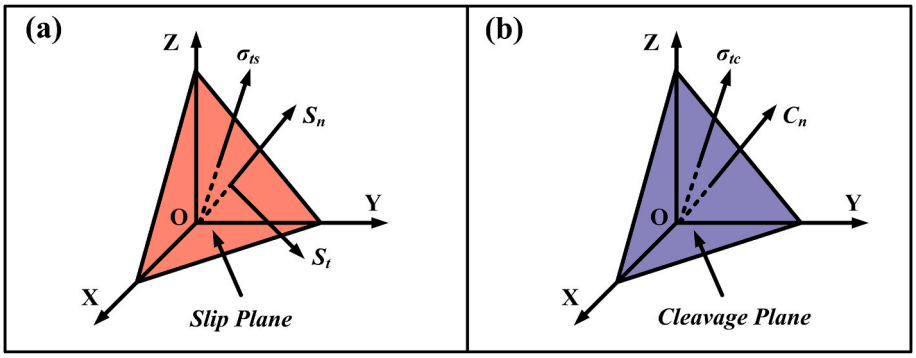

Fig. 3. Schematic of decomposed stress along (a) the slip systems and (b) the cleavage planes.

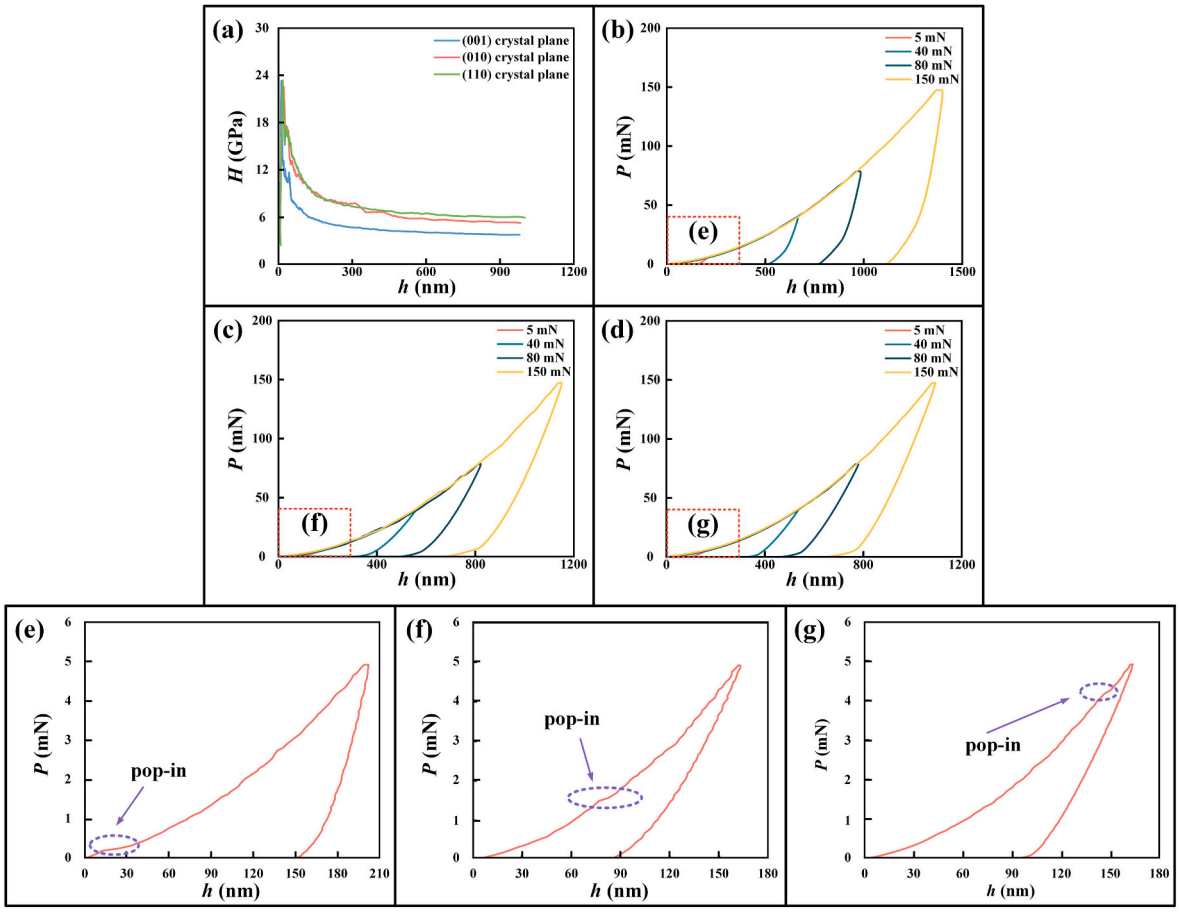

Fig. 4. (a) hardness curves of the (001), (010) and (110) crystal planes, displacement-load curves of (b) (001) crystal plane, (c) (010) crystal plane and (d) (110) crystal plane. (e), (f) and (g) are enlarged images of (b), (c) and (d), respectively.

$$\begin{cases} \sigma_s = \sigma_{ts}\cos\omega_s \\ \sigma_c = \sigma_{tc}\cos\omega_c \\ \cos\omega_s = \dfrac{\sigma_{ts}\cdot v_{st}}{|\sigma_{ts}|} \\ \cos\omega_c = \dfrac{\sigma_{tc}\cdot v_{cn}}{|\sigma_{tc}|} \end{cases} \tag{4}$$

where v_{st} is the unit vector which is along the slip direction S_t, v_{ct} is the unit vector which is perpendicular to the cleavage plane, ω_s is the angle between stresses σ_{ts} and v_{st}, and ω_c is the angle between stresses σ_{tc} and v_{cn}. The slip systems of MgF_2 single crystals are (110)/[001] and $(1\bar{1}0)$/[001] slip systems, and cleavage planes are (110) and $(1\bar{1}0)$ crystal planes [36]. To analyze the stress field simply, the stress is calculated by the normalized stress ($\sigma d^2/P$). d is the grid length and d = 2 nm.

2.3. The cleavage factors and schmid factors of S1, S2 and S3 surfaces

Due to the shape of Berkovich indenter, the activation degree of the slip motions and cleavage factors are different for S1, S2 and S3 surfaces. Therefore, the cleavage factors and Schmid factors of S1, S2 and S3 surfaces are calculated. The shape of Berkovich indenter is a triangular pyramid. The angle between the perpendicular line and edge line is 77.05°, and the angle between the perpendicular line and pyramid plane is 65.3°. Due to the geometry of Berkovich indenter, the forces that are applied to the workpiece by S1, S2 and S3 surfaces have the same value, and they are perpendicular to S1, S2 and S3 surfaces, respectively. $\overrightarrow{n_1}$, $\overrightarrow{n_2}$ and $\overrightarrow{n_3}$ are the normal vectors of the S1, S2 and S3 surfaces, respectively. m_i is the cleavage factor of the S*i* surface, which can be expressed by Equation (5),

$$m_i = \cos^2\alpha_i \tag{5}$$

where α_i is the angle between the S*i* surface and cleavage plane. $\cos\alpha_i$ can be expressed by Equation (6),

$$\cos\alpha_i = \frac{\overrightarrow{c_p}\,\overrightarrow{n_i}}{|\overrightarrow{c_p}||\overrightarrow{n_i}|} \tag{6}$$

where $\overrightarrow{c_p}$ is the normal vector of the cleavage plane, and μ_i is the Schmid factor of the S*i* surface. μ_i can be expressed by Equation (7),

$$\mu_i = \cos\lambda_i\cos\varphi_i \tag{7}$$

where λ_i is the angle between the S*i* surface and slip plane, and φ_i is the angle between the S*i* surface and slip direction. $\cos\lambda_i$ and $\cos\varphi_i$ can be expressed by Equation (8),

$$\begin{cases} \cos\lambda_i = \dfrac{\overrightarrow{s_i}\,\overrightarrow{s_p}}{|\overrightarrow{s_i}||\overrightarrow{s_p}|} \\ \cos\varphi_i = \dfrac{\overrightarrow{s_i}\,\overrightarrow{s_o}}{|\overrightarrow{s_i}||\overrightarrow{s_o}|} \end{cases} \tag{8}$$

m_i and μ_i can reflect the degree of the slip motions and cleavage fractures. The higher m_i and μ_i are, the more easily slip motions and cleavage fractures occur. Therefore, m_i and μ_i were used in Section 3.3 to reveal the deformation and damage behaviors of MgF_2 crystals under different conditions.

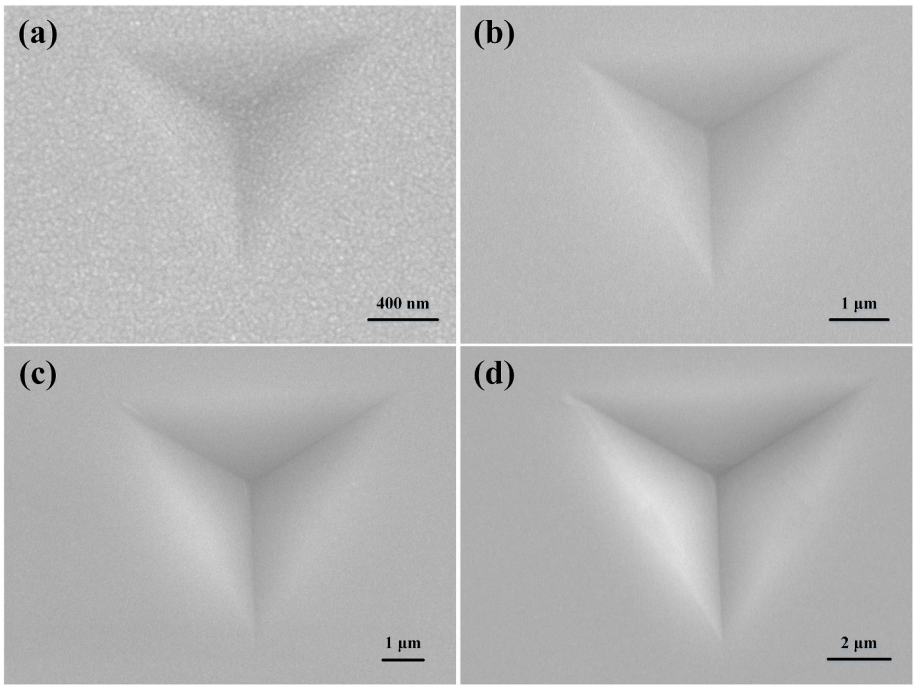

Fig. 5. The surface morphologies of the (001) crystal plane under the load of (a) 5 mN, (b) 40 mN, (c) 80 mN and (d) 150 mN.

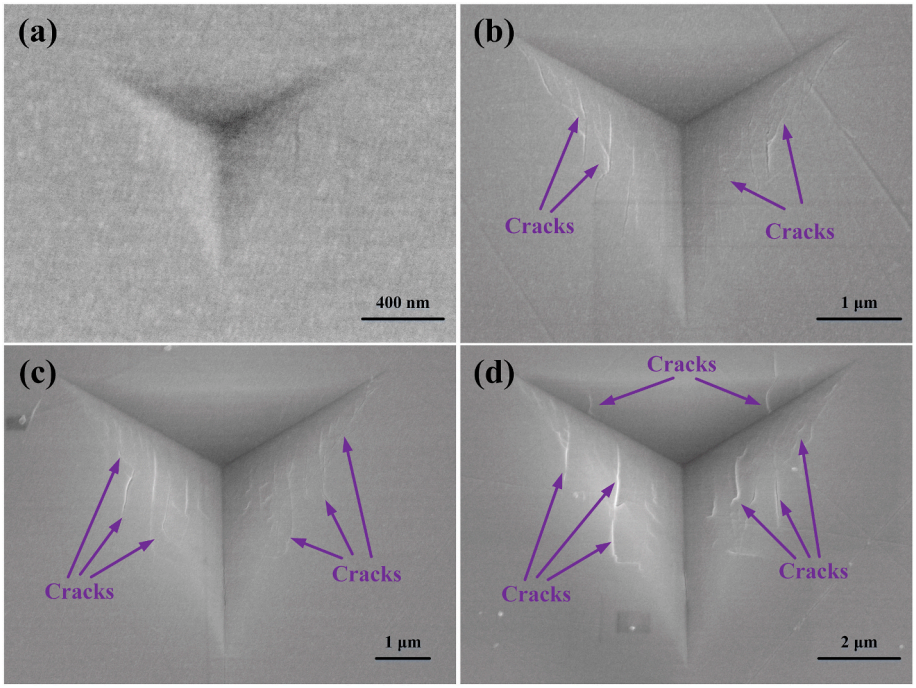

Fig. 6. Surface morphologies of the (010) crystal plane under the load of (a) 5 mN, (b) 40 mN, (c) 80 mN and (d) 150 mN.

3. Results and discussions

3.1. Deformation behaviors on different crystal planes

The hardness and the displacement-load curves of the (001), (010) and (110) crystal planes are shown in Fig. 4. With the indentation displacement h increasing, the hardness H of the (001), (010) and (110) crystal planes initially increases and then decreases. Similar results were reported due to the size effect [37,38]. When the indentation displacement h increases to approximately 600 nm, the hardness turns to be stable. The hardness of the (001), (010), and (110) crystal planes are approximately 3.93 GPa, 5.66 GPa and 6.20 GPa, respectively, indicating the significant differences in terms to the deformation behaviors. As shown in Fig. 4 (b)–(d), when the maximum load was 5 mN, the 'pop-in' phenomenon was observed on the (001), (010) and (110) crystal planes. Li et al. believed that the occurring 'pop-in' was the symbol of the elastic-to-plastic transition [39]. Therefore, the plastic deformation occurs on the (001), (010) and (110) crystal planes during the indentation process, and the critical loads of the first 'pop-in' for the (001), (010), and (110) crystal planes are 0.21 mN, 1.50 mN, and 4.18

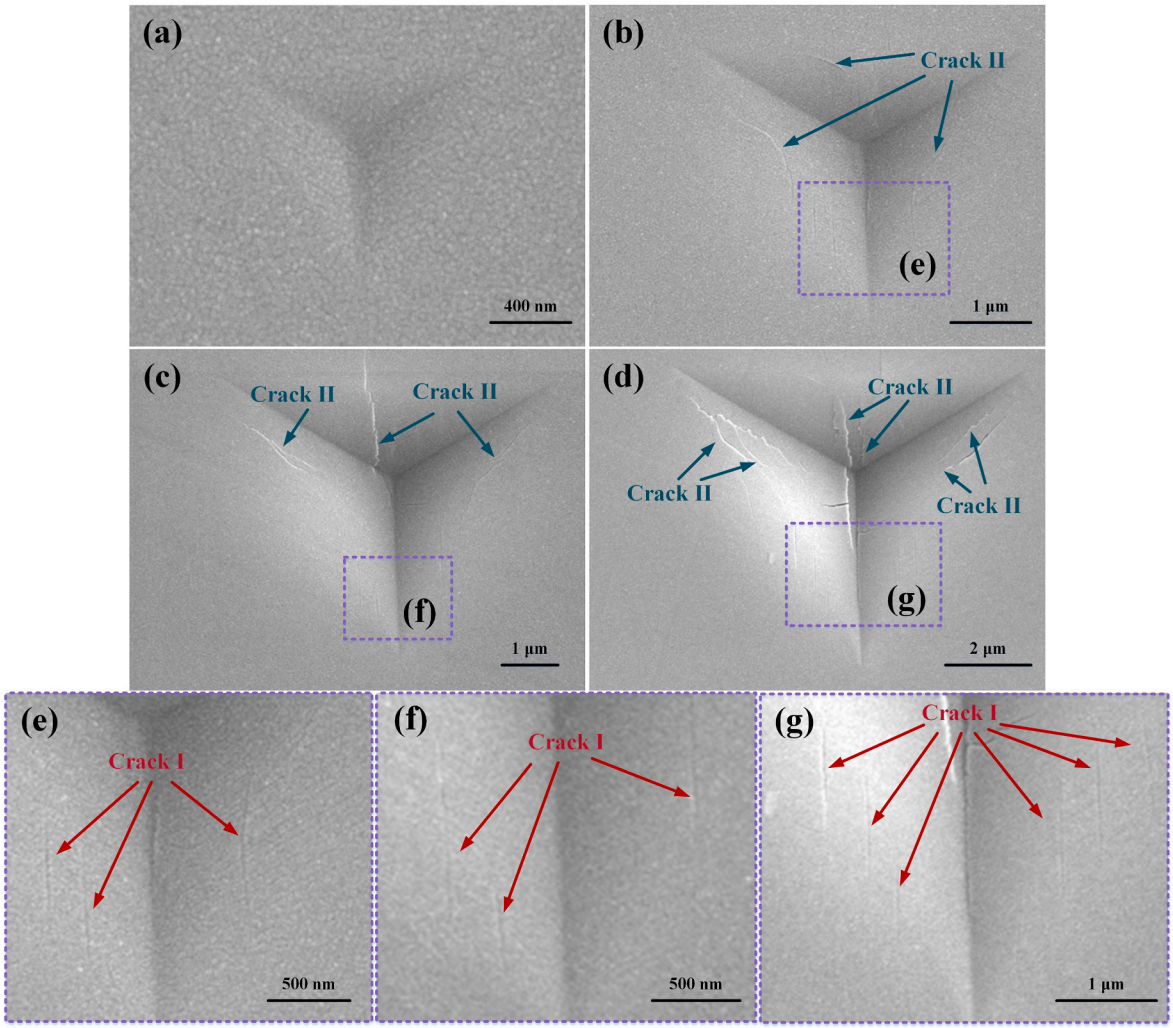

Fig. 7. Surface morphologies of the (110) crystal plane under the load of (a) 5 mN, (b) 40 mN, (c) 80 mN and (d) 150 mN. (e), (f) and (g) are enlarged images of (b), (c) and (d), respectively.

mN, respectively. When the load is a constant valve, the indentation displacement *h* of the (001) crystal plane is highest, but the indentation displacement *h* of (110) crystal plane is lowest.

The results of the hardness, load values of the first 'pop-in', and indentation displacement under the same load can reflect the plastic deformation behaviors [39,40]. The lower the hardness, the lower the load value of the first 'pop-in' and indentation displacement under the same load, and the more the plastic deformation. Therefore, the plastic deformation is most prone to occur on the (001) crystal plane and is hardest to occur on the (110) crystal plane.

The SEM images of the surface morphologies on the (001) crystal plane are shown in Fig. 5. Under the maximum loads of 5 mN, 40 mN, 80 mN and 150 mN, there were not distinct brittle fractures. Only the plastic deformation was found on the (001) crystal plane during the indentation process.

The SEM images of the surface morphologies on the (010) crystal plane are shown in Fig. 6. Only plastic deformation occurred on the (010) crystal plane when the maximum load was 5 mN. However, the cracks were generated on the S1 and S3 surfaces when the maximum load was 40 mN and 80 mN. With the maximum load increasing to 150 mN, cracks were occurred on the S2 surface, and the cracks propagated along [001] crystal orientation. However, the cracks mainly appeared on the S1 and S3 surfaces.

The SEM images of the surface morphologies on the (110) crystal plane are shown in Fig. 7. The plastic deformation was generated on the (110) crystal plane when the maximum load was 5 mN. When the maximum load was 40 mN, the cracks were appeared on the S1, S2 and S3 surfaces. The cracks were divided into two types, namely Crack I and Crack II. Crack I broke lightly and Crack II broke seriously. Crack I only appeared on the S1 and S3 surfaces, and propagated along the [001] crystal orientation. Crack II appeared on the S1, S2, and S3 surfaces. When the maximum load increased to 80 and 150 mN, both Crack I and Crack II continued to propagate. However, Crack I only generated on the S1 and S3 surfaces.

According to the SEM images, it is clear that the anisotropy of the deformation behaviors is significantly obvious. The cracks are only found on the (010) and (110) crystal planes. For the (010) crystal plane, the cracks mainly generated on the S1 and S3 surfaces, and the cracks of S1, S2 and S3 surfaces propagated along the [001] crystal orientation. For the (110) crystal plane, two types of cracks are observed, and Crack I was only observed on the S1 and S3 surfaces with propagating along the [001] crystal orientation.

3.2. Stress distribution of different crystal planes

The stress simulation results along XOY plane were calculated and *z* is 100 nm. Normalized stress along the slip systems is shown in Fig. 8. Fig. 8(a1) and (a2) shows that both tensile and compressive stresses appear on the (001) crystal plane with the symmetric distribution. Consequently, the slip activated degrees of the (110)/[001] and

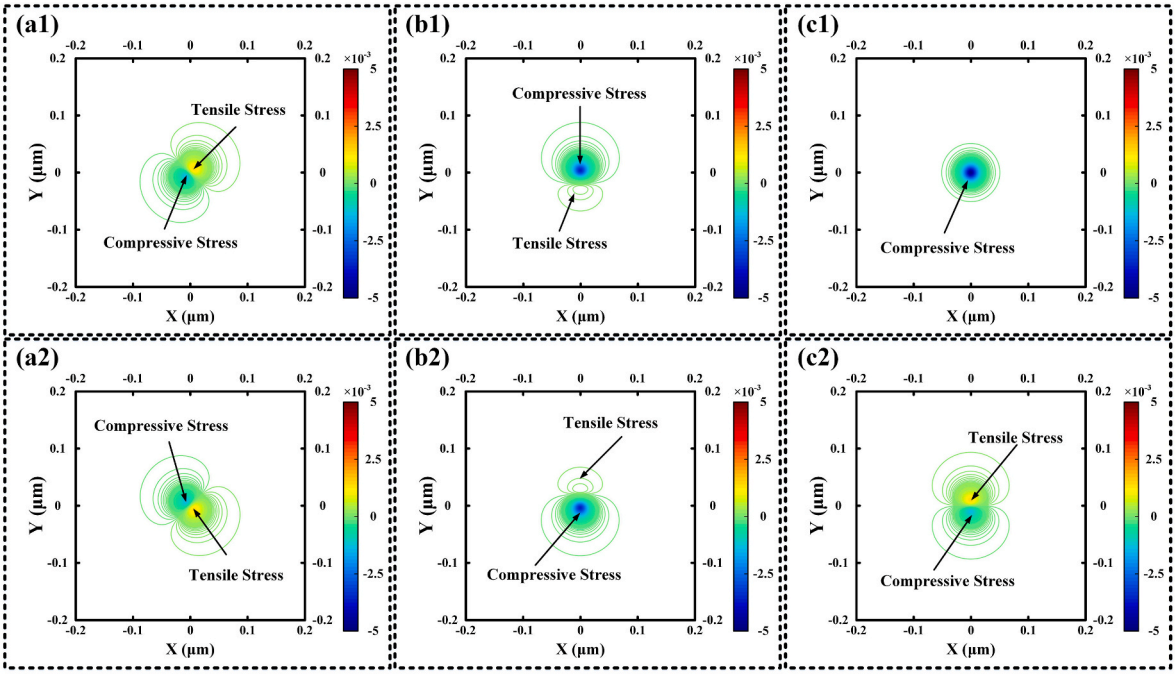

Fig. 8. (a1), (b1) and (c1) are the normalized stresses along (110)/[001] slip system on the (001), (010) and (110) crystal planes, respectively. (a2), (b2) and (c2) are the normalized stresses along $(1\bar{1}0)$/[001] slip system on the (001), (010) and (110) crystal planes, respectively.

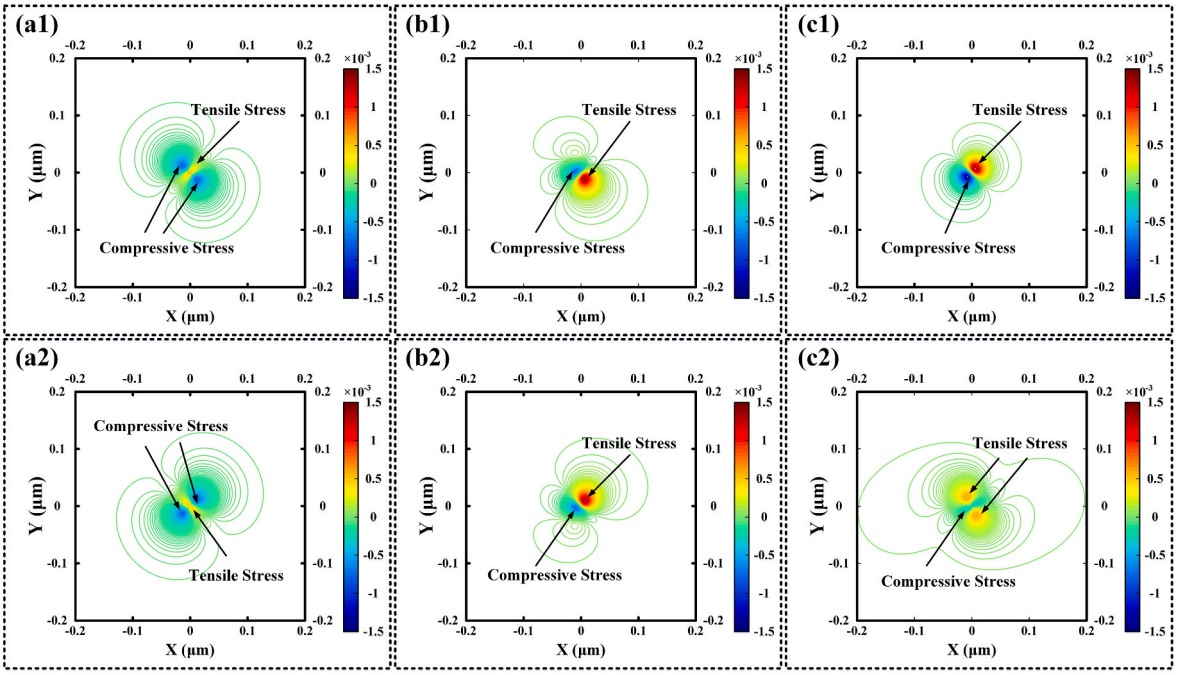

Fig. 9. (a1), (b1) and (c1) are the normalized stresses perpendicular to the (110) cleavage plane on (001), (010) and (110) crystal planes, respectively. (a2), (b2) and (c2) are the normalized stresses perpendicular to the $(1\bar{1}0)$ cleavage plane on (001), (010) and (110) crystal planes, respectively.

$(1\bar{1}0)$/[001] slip systems are the same on the (001) crystal plane. As shown in Fig. 8(b1) and (b2), the stress is mainly concentrated on the one side, which indicates that the distribution of the slip motions is uneven. The results of Fig. 8(b1) and (b2) are symmetrical, which indicates that the slip activated degrees of the (110)/[001] and $(1\bar{1}0)$/[001] slip systems are the same. As shown in Fig. 8(c1) and (c2), the differences between Fig. 8(c1) and Fig. 8(c2) are significant, and the stress value and area of the $(1\bar{1}0)$/[001] slip system are larger and more even than those of the (110)/[001] slip system, resulting in that the slip activated degree of the (110)/[001] slip system is less than that of the $(1\bar{1}0)$/[001] slip system. Consequently, the slip motion mainly occurs on the $(1\bar{1}0)$/[001] slip system.

Compared with the simulated results, the (110)/[001] and $(1\bar{1}0)$/[001] slip systems are activated with the same degree on the (001) and (010) crystal planes. However, the $(1\bar{1}0)$/[001] slip system is mainly activated on the (110) crystal plane. As reported by Li [41] et al.,

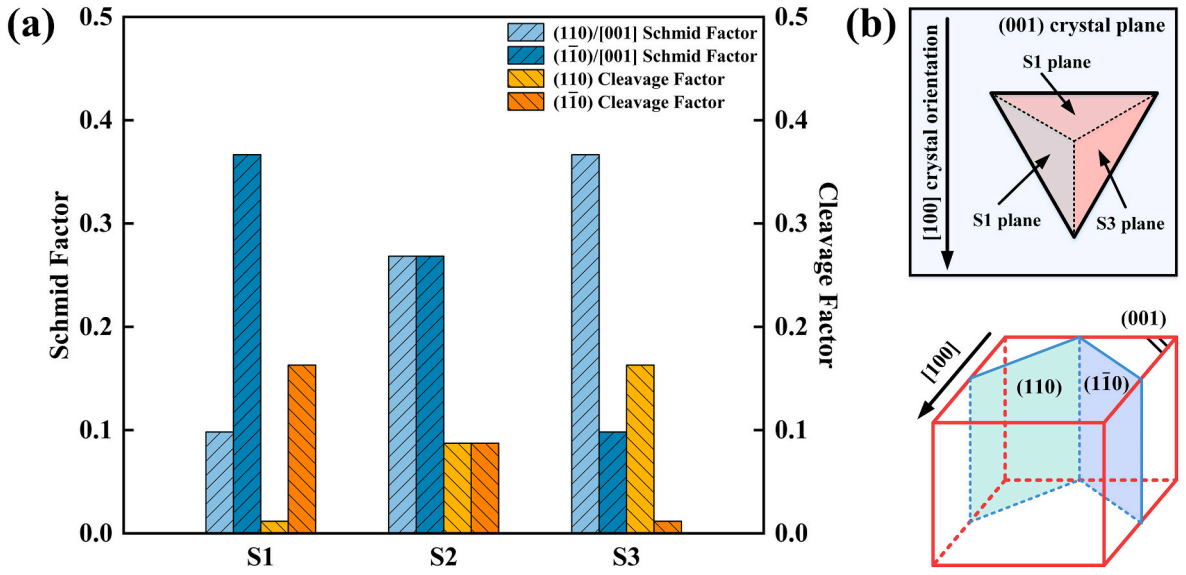

Fig. 10. (a) Cleavage factors and Schmid factors of S1, S2 and S3 planes on (001) crystal plane, (b) the spatial relationship among cleavage plane, slip plane and indenter on (001) crystal plane.

increasing the number of the activated slip systems will contribute to the plastic deformation. Therefore, the plastic deformation is hard to occur on the (110) crystal plane. Besides, the stress distribution area of the (001) crystal plane is larger and more even than those of the (010) crystal plane, which indicates that the area of the slip motions on the (001) crystal plane is larger and more even than those of the (010) crystal plane. Therefore, the plastic deformation is more prone to occur on the (001) crystal plane.

The stress along the cleavage planes is shown in Fig. 9. Fig. 9(a1) and (a2) shows that the stress which is perpendicular to the (110) and (1$\bar{1}$0) cleavage plane is compressive stress on the (001) crystal plane. The cleavage fractures are induced by the tensile stress. Therefore, the cleavage fractures are hard to generate on the (001) crystal plane. The stress distribution area is similar between Fig. 9(b1) and Fig. 9(b2), which indicates that the degrees of cleavage fractures along the (110) and (1$\bar{1}$0) cleavage planes are the same. At the same time, the stress is mainly tensile stress, resulting in the generation of cleavage fractures along the (110) and (1$\bar{1}$0) cleavage planes. In Fig. 9(c1) and (c2), the area and value of the tensile stress along the (110) cleavage plane are much larger than those along the (1$\bar{1}$0) cleavage plane, which illustrates that the cleavage fracture mainly occurs along the (110) cleavage plane.

Compared with the results of Fig. 9, the value of the tensile stress on the (001) crystal plane is less than that on the (010) and (110) crystal planes. Therefore, there are obvious cracks on the (010) and (110) crystal planes, and no brittle fracture occurs on the (001) crystal plane. The area and values of the tensile stress on the (010) crystal plane are larger than those on the (110) crystal plane. Therefore, brittle fractures are severer on the (010) crystal plane, which is consistent with the experiment result.

3.3. Cleavage factors and schmid factors of S1, S2 and S3 surfaces

The anisotropy of the atomic arrangement along different orientations leads to different clearance factors and Schmid factors on different

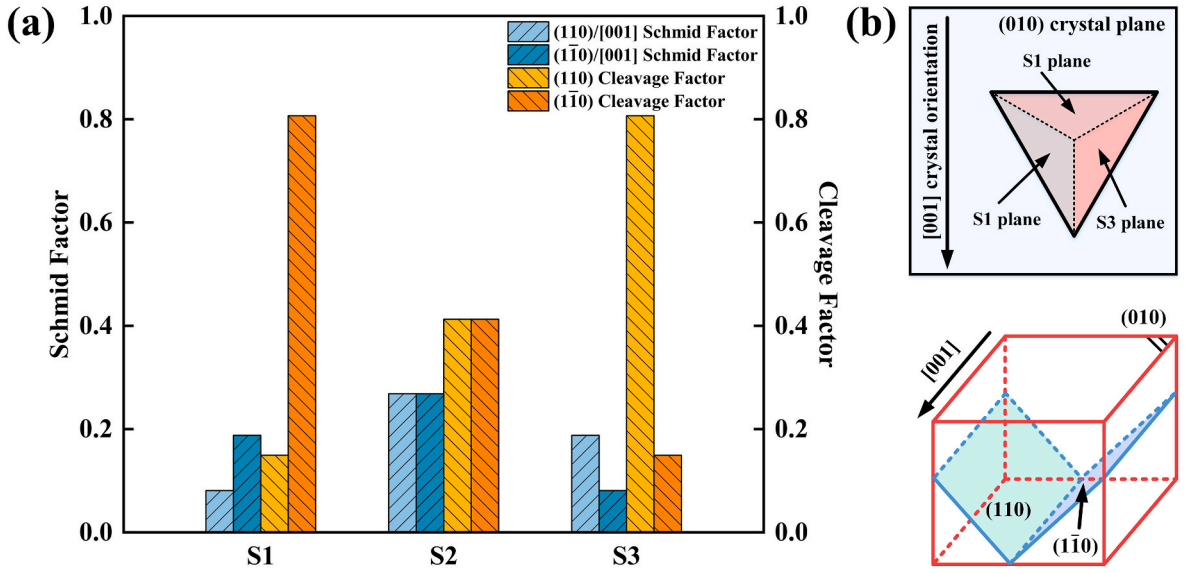

Fig. 11. (a) Cleavage factors and Schmid factors of S1, S2 and S3 planes on (010) crystal planes, (b) the spatial relationship among cleavage plane, slip system and indenter on (010) crystal planes.

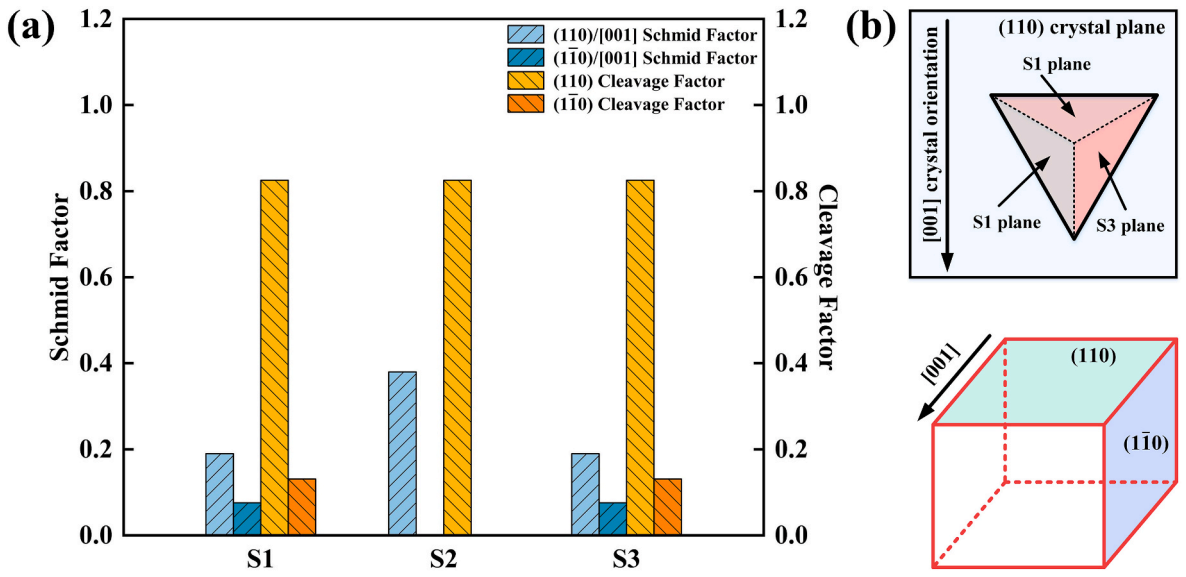

Fig. 12. (a) Cleavage factors and Schmid factors of S1, S2 and S3 planes on (110) crystal plane, (b) the spatial relationship among cleavage plane, slip system and indenter on (110) crystal plane.

crystal planes [42,43]. Cleavage factors and Schmid factors of the (001) crystal plane are shown in Fig. 10. The maximum Schmid factors of the S1, S2 and S3 surfaces are significantly higher than the maximum cleavage factors of the S1, S2 and S3 surfaces, which indicates that slip motions are more prone to occur on the (001) surface. The slip motions can inhibit the initiation and propagation of the cracks. Therefore, there is no obvious crack on the S1, S2 and S3 surfaces. For the S1 surface, the Schmid factor of the (1$\bar{1}$0)/[001] slip system is much higher than that of the (110)/[001] slip system, illustrating that the slip motions of the S1 surface are dominated by the (1$\bar{1}$0)/[001] slip system. Similarly, Schmid factors of the (110)/[001] and (1$\bar{1}$0)/[001] slip systems are equal for the S2 surface, and Schmid factors of the (110)/[001] slip system are much higher than those of the (1$\bar{1}$0)/[001] slip system, which indicates that the slip motions of the S2 surface are dominated by the (110)/[001] and (1$\bar{1}$0)/[001] slip systems, and the slip motions of the S3 surface are dominated by the (110)/[001] slip system.

Cleavage factors and Schmid factors of the (010) crystal plane are shown in Fig. 11. For the S1, S2 and S3 surfaces, the maximum cleavage factors are higher than the maximum Schmid factors, which indicates that the cleavage fractures are dominant. However, the maximum cleavage factors of the S1 and S3 surfaces are 0.81, and the maximum cleavage factor of S2 surface is 0.41. Besides, the Schmid factors of the (1$\bar{1}$0)/[001] and (110)/[001] slip systems are higher than those of the S1 and S2 surfaces. The higher Schmid factors and lower cleavage factors illustrates that the cracks are hard to be generated on the S2 surface. Therefore, the cracks are preferentially and mainly appeared on the S1 and S3 surfaces. The (1$\bar{1}$0) cleavage factor is the largest for the S1 surface, and the (110) cleavage factor is the largest for the S3 surface. Cleavage factors of the (1$\bar{1}$0) and (110) cleavage planes are the same for the S2 surface. Consequently, the cracks of the S1 surface propagate along the (1$\bar{1}$0) cleavage plane, and the cracks of the S3 surface propagate along the (110) cleavage plane. The cracks of the S2 surface will propagate along the (1$\bar{1}$0) and (110) cleavage planes. According to Figs. 6 and 11(b), the results of the cracks propagation are consistent with the simulated results. The spatial relationship among the S1 surface, S3 surface, cleavage planes and slip systems is shown in Fig. 11(b). Despite the activations of slip systems and cleavage fractures for the S1 and S3 surfaces are different, it is symmetric in term of the slip systems and cleavage planes for the S1 and S3 surfaces. Therefore, the deformation behaviors of the S1 and S3 planes are the same, which is consistent with the experimental result.

Cleavage factors and Schmid factors of the (110) crystal plane are shown in Fig. 12. The maximum cleavage factors of the S1, S2 and S3 surfaces are the same and are significantly higher than Schmid factors of the S1, S2 and S3 surfaces. Consequently, the cracks are prone to be generated during the nanoindentation process. The cleavage factors of (110) crystal plane are higher than those of (1$\bar{1}$0) crystal plane for the S1, S2 and S3 surfaces, illustrating that Crack II is induced by the cleavage fractures along the (110) cleavage plane, and Crack I is induced by the cleavage fractures along the (1$\bar{1}$0) cleavage plane. At the same time, the (1$\bar{1}$0) cleavage factor for the S2 surface is 0. Therefore, Crack I is hard to appear on the S2 surface. The cleavage factors and Schmid factors of the S1 and S3 surfaces are the same. Therefore, the deformation behaviors of the S1 and S3 surfaces are the same, which is consistent with the experimental result.

4. Conclusions

This work systematically carries out the nanoindentation tests of the MgF_2 single crystal, and the surface morphologies under different experimental conditions were analyzed. The stress, cleavage factors and Schmid factors were calculated to successfully reveal the anisotropy of the deformation behaviors by competition between the slip motions and cleavage fractures. The following conclusions can be obtained.

- The hardness, the displacement-load curves and the surface morphologies of the MgF_2 single crystal were obtained by the nanoindentation tests and the SEM. The hardness, the load values of the first occurrence of 'pop-in', indentation displacement indicate the (001) crystal plane is most prone to occur the plastic deformation and the (110) crystal plane is hardest to occur the plastic deformation. The SEM images of the surface morphologies indicates that cracks break most severely on the (010) crystal plane.
- The stress model induced by the nanoindentation was developed, and the stress was decomposed along the slip systems and the cleavage planes of the MgF_2 single crystal. Under the same experimental conditions, the nanoindentation of the (001) crystal plane activated most slip motions, so the plastic deformation is most prone to occur on the (001) crystal plane. However, the nanoindentation the (110) crystal plane activated fewest slip motions, so the plastic deformation is hardest to occur on the (110) crystal plane. The

nanoindentation of the (010) crystal plane activated less slip motions and most cleavage fractures, so the brittle fractures are severest on the (010) crystal plane.

- The Schmid factors and the cleavage factors of the S1, S2 and S3 surfaces were calculated to deeply analyzed the anisotropy of the deformation behaviors. Due to the different activation degrees of the slip motions and cleavage fractures, the surface morphologies of the S1, S2 and S3 surfaces were significant different from each other. For the (001) crystal plane, only plastic deformation was generated. For the (010) crystal plane, the cracks propagated along the cleavage planes, and the cracks were preferentially and mainly generated on the S1 and S3 surfaces. For the (110) crystal plane, Crack II was induced by the (110) cleavage fractures the Crack I was induced by the $(1\bar{1}0)$ cleavage fractures. The Crack II broken more seriously than the Crack I due to the higher activation degree of the cleavage fractures.

Declaration of competing interest

The authors declare that they have no known competing financial interests or personal relationships that could have appeared to influence the work reported in this paper.

Acknowledgment

This work was supported by the National Natural Science Foundation of China (52375420, 52005134), Natural Science Foundation of Heilongjiang Province of China (YQ2023E014), Self-Planned Task (No. SKLRS202214B) of State Key Laboratory of Robotics and System (HIT), China Postdoctoral Science Foundation (2022T150163), Young Elite Scientists Sponsorship Program by CAST (No. YESS20220463), Open Fund of Key Laboratory of Microsystems and Microstructures Manufacturing (HIT) (2022KM004), and Fundamental Research Funds for the Central Universities (Grant No. HIT. OCEF.2022024, FRFCU5710051122).

References

[1] Yu DP, Wong YS, Hong GS. A novel method for determination of the subsurface damage depth in diamond turning of brittle materials. Int J Mach Tool Manufact 2011;51(12):918–27.
[2] Huang W, Yu D, Zhang M, Cao Q, Yao J. Predictive cutting force model for ductile-regime machining of brittle materials. Int J Adv Des Manuf Technol 2018;98:781–90.
[3] Babu KR, Lingam CB, Auluck S, Tewari SP, Vaitheeswaran G. Structural, thermodynamic and optical properties of MgF2 studied from first-principles theory. J Solid State Chem 2011;184(2):343–50.
[4] Wei J, He Y, Wang F, He Y, Rong X, Chen M, Wang Y, Yue H, Liu J. Convolutional neural network assisted infrared imaging technology: an enhanced online processing state monitoring method for laser powder bed fusion. Infrared Phys Technol 2023;131:104661.
[5] Qu S, Yao P, Gong Y, Chu D, Yang Y, et al. Environmentally friendly grinding of C/SiCs using carbon nanofluid minimum quantity lubrication technology. Journal of Cleaner Production 2022;366:132898.
[6] Kumar S, Tong Z, Jiang X. Advances in the design and manufacturing of novel freeform optics. Int J Extrem Manuf 2022;4(3):032004.
[7] Lou Z, Yan Y, Wang J, Zhang A, Cui H, Li C, et al. Exploring the structural color of micro-nano composite gratings with FDTD simulation and experimental validation. Optics Express 2024;32(2):2432-2451.
[8] Hayama Y, Fujii S, Tanabe T, Kakinuma Y. Theoretical approach on the critical depth of cut of single crystal MgF_2 and application to a microcavity. Precis Eng 2022;73:234–43.
[9] Min S, Dornfeld D, Inasaki I, Ohmori H, Lee D, Deichmueller M, Yasuda T, Niwa K. Variation in machinability of single crystal materials in micromachining. CIRP annals 2006;55(1):103–6.
[10] Liu X, Yu D, Chen D, Yang S, Wen Y, Xiao Y. Self-tuned ultrasonic elliptical vibration cutting for high-efficient machining of micro-optics arrays on brittle materials. Precis Eng 2021;72:370–81.
[11] Li C, Zhang Q, Zhang Y, Zhang F, Wang X, Dong G. Nanoindentation and nanoscratch tests of YAG single crystals: an investigation into mechanical properties, surface formation characteristic, and theoretical model of edge-breaking size. Ceram Int 2020;46(3):3382–93.
[12] Liu Q, Liao Z, Axinte D. Temperature effect on the material removal mechanism of soft-brittle crystals at nano/micron scale. Int J Mach Tool Manufact 2020;159:103620.
[13] Liu Q, Chen M, Liao Z, Feng J, Xu D, Cheng J. On the improvement of the ductile removal ability of brittle KDP crystal via temperature effect. Ceram Int 2021;47(23):33127–39.
[14] Yan J, Takahashi H, Gai X, Harada H, Tamaki JI, Kuriyagawa T. Load effects on the phase transformation of single-crystal silicon during nanoindentation tests. Mater Sci Eng 2006;423(1–2):19–23.
[15] Zhang Y, Hou N, Zhang LC. Investigation into the room temperature creep-deformation of potassium dihydrogen phosphate crystals using nanoindentation. Adv Manu 2018;6:376–83.
[16] Csanádi T, Németh D, Dusza J, Lenčéš Z, Šajgalík P. Nanoindentation induced deformation anisotropy in β-Si3N4 ceramic crystals. J Eur Ceram Soc 2016;36(12):3059–66.
[17] Li C, Piao Y, Meng B, Zhang Y, Li L, Zhang F. Anisotropy dependence of material removal and deformation mechanisms during nanoscratch of gallium nitride single crystals on (0001) plane. Appl Surf Sci 2022;578:152028.
[18] Wang J, Yan Y, Li C, Geng Y. Material removal mechanism and subsurface characteristics of silicon 3D nanomilling. Int J Mech Sci 2023;242:108020.
[19] Meng Binbin, Chen Li. Effect of anisotropy on deformation and crack formation under the brittle removal of 6H-SiC during SPDT process. J Adv Res 2023. https://doi.org/10.1016/j.jare.2023.04.004.
[20] Yan J, Syoji K, Kuriyagawa T, Suzuki H. Ductile regime turning at large tool feed. J Mater Process Technol 2002;121(2–3):363–72.
[21] Huang W, Nagayama K, Yan J. Fabrication of microlens arrays on single-crystal CaF_2 by ultraprecision diamond turning. J Mater Process Technol 2023;321:118133.
[22] Huang S, Lin J, Wang N, Guo B, Jiang F, Wen Q, Lu X. Fracture behavior of single-crystal sapphire in different crystal orientations. Crystals 2021;11(8):930.
[23] Li H, Jensen M, Bradt RC. Microhardness anisotropy on the (010) cleavage plane of single crystals of Bi_2S_3 and Sb_2S_3. J Mater Sci 1992;27:1357–60.
[24] Kwon SB, Nagaraj A, Yoon HS, Min S. Study of material removal behavior on R-plane of sapphire during ultra-precision machining based on modified slip-fracture model. Nanotechnology and Precision Engineering 2020;3(3):141–55.
[25] Mizumoto Y, Kakinuma Y. Revisit of the anisotropic deformation behavior of single-crystal CaF_2 in orthogonal cutting. Precis Eng 2018;53:9–16.
[26] Li X, Gao Y, Ge P, Zhang L, Bi W, Meng J. Nucleation location and propagation direction of radial and median cracks for brittle material in scratching. Ceram Int 2019;45(6):7524–36.
[27] Yang X, Qiu Z, Li X. Investigation of scratching sequence influence on material removal mechanism of glass-ceramics by the multiple scratch tests. Ceram Int 2019;45(1):861–73.
[28] Li C, Hu Y, Zhang F, Geng Y, Meng B. Molecular dynamics simulation of laser assisted grinding of GaN crystals. Int J Mech Sci 2023;239:107856.
[29] Li C, Piao Y, Meng B, Hu Y, Li L, Zhang F. Phase transition and plastic deformation mechanisms induced by self-rotating grinding of GaN single crystals. Int J Mach Tool Manufact 2022;172:103827.
[30] Wang P, Ge P, Ge M, Bi W, Meng J. Material removal mechanism and crack propagation in single scratch and double scratch tests of single-crystal silicon carbide by abrasives on wire saw. Ceram Int 2019;45(1):384–93.
[31] Wang P, Ge P, Bi W, Liu T, Gao Y. Stress analysis in scratching of anisotropic single-crystal silicon carbide. Int J Mech Sci 2018:141 1–8.
[32] Li X, Gao Y, Ge P, Zhang L, Bi W, Meng J. Nucleation location and propagation direction of radial and median cracks for brittle material in scratching. Ceram Int 2019;45(6):7524–36.
[33] Li C, Piao Y, Zhang F, Zhang Y, Hu Y, Wang Y. Understand anisotropy dependence of damage evolution and material removal during nanoscratch of MgF_2 single crystals. Int J Extrem Manuf 2023;5:015101.
[34] Mizumoto Y, Maas P, Kakinuma Y, Min S. Investigation of the cutting mechanisms and the anisotropic ductility of monocrystalline sapphire. CIRP Annals 2017;66(1):89–92.
[35] Wang J, Guo B, Zhao Q, Zhang C, Zhang Q, Chen H, Sun J. Dependence of material removal on crystal orientation of sapphire under cross scratching. J Eur Ceram Soc 2017;37(6):2465–72.
[36] Fujii S, Hayama Y, Imamura K, Kumazaki H, Kakinuma Y, Tanabe T. All-precision-machining fabrication of ultrahigh-Q crystalline optical microresonators. Optica 2020;7(6):694–701.
[37] Zhao J, Wang F, Huang P, Lu TJ, Xu KW. Depth dependent strain rate sensitivity and inverse indentation size effect of hardness in body-centered cubic nanocrystalline metals. Mater Sci Eng 2014;615:87–91.
[38] Limbach R, Kosiba K, Pauly S, Kühn U, Wondraczek L. Serrated flow of CuZr-based bulk metallic glasses probed by nanoindentation: role of the activation barrier, size and distribution of shear transformation zones. J Non-Cryst Solids 2017;459:130–41.
[39] Li C, Zhang F, Wang X, Rao X. Investigation on surface/subsurface deformation mechanism and mechanical properties of GGG single crystal induced by nanoindentation. Appl Opt 2018;57(14):3661–8.
[40] Huang Shuiquan, Gao Shang, Huang Chuanzhen, Huang Han. Nanoscale removal mechanisms in abrasive machining of brittle solids. Diam Abrasives Eng 2022;42(3):257–267+384. https://doi.org/10.13394/j.cnki.jgszz.2021.3009.

[41] Li C, Zhang F, Piao Y. Strain-rate dependence of surface/subsurface deformation mechanisms during nanoscratching tests of GGG single crystal. Ceram Int 2019;45 (12):15015–24.

[42] Wang Chao, Ge Peiqi, He Jikai, Wang Xinhui. Influence of crystal anisotropy and process parameters on surface shape deviation of sapphire slicing. Diam Abrasives Eng 2023;43(5):612–20. https://doi.org/10.13394/j.cnki.jgszz.2022.0207.

[43] Huang W, Yan J. Effect of tool geometry on ultraprecision machining of soft-brittle materials: a comprehensive review. Int J Extrem Manuf 2023;5(1):012003.